Journal of Applied Polymer Science

Failure behavior of resorcinol–formaldehyde latex coated aramid short-fiber-reinforced rubber sealing under transverse tension

Bin Zhang, Boqin Gu, Xiaoming Yu
School of Mechanical and Power Engineering, Nanjing Tech University, Nanjing, 211816, China
Correspondence to: B. Gu (E-mail: bqgu@njtech.edu.cn)

ABSTRACT: Composites composed of rubber, sepiolite fiber, and resorcinol–formaldehyde latex-coated aramid short fibers were prepared. Mechanical and morphological characterizations were carried out. To investigate the effect of interfacial debonding on the failure behavior of short-fiber-reinforced rubber composites, a micromechanical representative volume element model for the composites was developed. The cohesive zone model was used to analyze the interfacial failure. We found that computational results were in good agreement with the experimental results when the interfacial fracture energy was 1 J/m^2 and the interfacial strength was 10 MPa. A parametrical study on the interface and interphase of the composite was conducted. The results indicate that a good interfacial strength and a choice of interphase modulus between 40 and 50 MPa enhanced the ductile behavior and strength of the composite. The ductile properties of the composite also increased with increasing interfacial fracture energy. © 2014 Wiley Periodicals, Inc. J. Appl. Polym. Sci. **2015**, *132*, 41672.

KEYWORDS: composites; fibers; mechanical properties; rubber; surfaces and interfaces

Received 16 July 2014; accepted 20 October 2014
DOI: 10.1002/app.41672

INTRODUCTION

Generally, short fibers mixed into elastomers contribute to the improvement in the hardness,[1] heat buildup, and wear properties[2] and, therefore, increase the durability of the corresponding applications. Short fibers in elastomers can provide a substantial contribution to the building of more efficient and durable tires, conveyor belts, seals, and hoses. In these applications, interfacial debonding is a common damage that greatly affects their mechanical behavior and, hence, must be properly taken into account. To achieve the optimal transfer of loads and stresses from the matrix to the reinforced material, the adhesion between the fiber and matrix should be optimized. Among the fibers, the short aramid fibers can offer a good reinforcement level in elastomers because of their unique combination of stiffness, strength, toughness, and thermal resistance.[3–5]

The fibers were treated in different ways to achieve better bonding between the elastomers and fibers.[6–9] Resorcinol–formaldehyde latex (RFL) based dipping systems have been developed for the improvement of adhesion between, for example, rayon or polyamide fibers and natural rubber systems. In these applications, the RFL dip can be applied directly onto the fibers.[10,11] The chemical interaction between the resorcinol–formaldehyde (RF) portion of the RFL dip and the available functional groups on the rayon or polyamide fiber leads, after curing, to high fiber-dip adhesion. The latex portion of the RFL dip is responsible for further interactions with the rubber system.[12] Untreated aramid fibers, however, show almost no interaction with the RFL dip because of a lack of reactive functional groups on the surface and the high crystallinity of the fiber. This implies very weak fiber–rubber adhesion when the RFL dip is directly applied to the untreated aramid. Therefore, aramid fibers are generally predipped in an epoxy-based dipping system to improve the interactions between the fibers and RFL. This leads to sufficient adhesion in aramid-reinforced rubber applications.[13–16]

The stress-transfer mechanisms between the matrix and fiber and the interfacial properties for reinforced thermoplastic materials are becoming exceptionally important because of their ease of fabrication and reduced manufacturing costs.[9] A number of micromechanical tests have been developed to determine the effective adhesion and stress transfer from the matrix to the fibers in the composites. The most commonly used tests on single-fiber composites are the fiber fragmentation test, the microdebonding test, and the single-fiber pullout test.[17] Because, in most cases, the damage process in unidirectional composites begins at the constituent level, a realistic failure analysis should start at the same level. Unfortunately, accurate measurement of the local strain and stress distributions throughout the microstructure is practically impossible

Table I. Component Proportion of SFRC

Component	Weight content (wt %)
NBR-3345	21
Aramid fiber	28
Sepiolite fiber	49
Sulfur	0.4
ZnO	0.5
Stearic acid	0.2
Accelerating agent	0.4
Antiaging agent	0.5

by experimental methods. Therefore, the development of micromechanics models that on the one hand, take into account microstructural effects and, on the other hand, link the macroscopic behavior of unidirectional composites to the microstructural phenomena occurring inside it is essential. An efficient way to analyze the microstructural influences on the load-bearing behavior of such materials is the use of the numerical technique of homogenization based on the unit cell approach and the finite element method.[18–20] According to this technique, different phases in a composite, such as the matrix, fibers, and interphase, are explicitly modeled by finite elements, and their material properties are directly assigned to the elements.

Romanowicz,[21,22] Kushch *et al.*,[23] and Yang *et al.*[24] have presented computational models for estimating the strength of fiber-reinforced composites subjected to a transverse tensile load. The complex damage mechanism, including the fiber/matrix debonding and matrix plastic deformation, was discussed. Vaughan and McCarthy[25] analyzed the effect of fiber–matrix debonding and thermal residual stress on the transverse damage behavior of unidirectional carbon fiber-reinforced epoxy composites. A three-dimensional micromechanical unit cell model of the composites was developed by Mishnaevsky and Brøndsted,[26] where the effect of the statistical variability of fiber strengths, the viscosity of the polymer matrix, and the interaction between the damage processes in the matrix, fibers, and interface was investigated. The strain-rate-dependent transverse tensile failure of the unidirectional composites was numerically studied by Koyanagi *et al.*[27] They showed that the failure mode depended on the strain rate, with an interface-failure-dominant mode at a relatively high strain rate and a matrix-failure-dominant mode at a relatively low strain rate. In the aforementioned micromechanical model, the cohesive zone model of interface was adopted to analyze the nucleation, onset, and growth of an interfacial crack.

Table II. Physicomechanical Specifications of the Aramid Short Fibers

Average aspect ratio	250
Average fiber length (mm)	3
Tensile modulus (GPa)	20–21
Tensile strength (MPa)	3000–3250
Elongation at break (%)	5–7

Table III. Component of the RFL Latex System

Component	Dry part (g)	Wet part (g)
RF solution		
Resorcinol	4.0	4.0
Formaldehyde	2.2	6.0
Sodium hydroxide	0.2	2.0
Soft water	—	88.0
Age 6 h at 25°C	6.4	100.0
Latex compound		
Butadiene–vinyl pyridine copolymer latex	27.5	74.4
SB latex	7.7	20.9
Ammoniacal liquor	—	4.7
Age 20 h at 25°C	35.2	100.0

Until now, much work has been done on the development, performance evaluation, and engineering application of the sealing composites reinforced with aramid fibers, and many results have been achieved. However, the characterization of the microstructural parameters and the mechanical analysis and macroperformance prediction of these materials according to the micromechanical model are still very scarce. In this study, a sample of short-fiber-reinforced rubber composites (SFRCs) was prepared. The transverse tensile strength was adopted to evaluate the degree of adhesion between aramid fibers and the rubber matrix. The fractured surfaces of the samples were analyzed with scanning electron microscopy (SEM). Then, a micromechanical representative volume element (RVE) model of SFRC was developed. Appropriate cohesive element parameters were chosen to analyze the debonding process. The effects of the interfacial parameters and the interphase modulus on the debonding process are discussed. The results show that both interfacial parameters and the interphase modulus had a remarkable influence on the damage evolution of SFRC.

EXPERIMENTAL

Materials

Acrylonitrile–butadiene rubber (NBR; NBR-3345) is copolymer of acrylonitrile (31–35%) and butadiene-1.3 and a conventional sulfur curing additive were purchased from Nanjing Rubber Co. Sepiolite fibers were obtained from Hefei Asbestos Co. Aramid short-fiber Technora-T323SB (chopped fibers) was provided by Teijin-Twaron. Styrene–butadiene (SB) copolymer latex and butadiene–vinyl pyridine copolymer latex were provided by Zibo Qilong Chemical Co. Other chemicals were purchased from Nanjing Chemical Reagents Co. The component proportions of SFRC are given in Table I. The physicomechanical properties of the aramid short fibers are listed in Table II.[2,14]

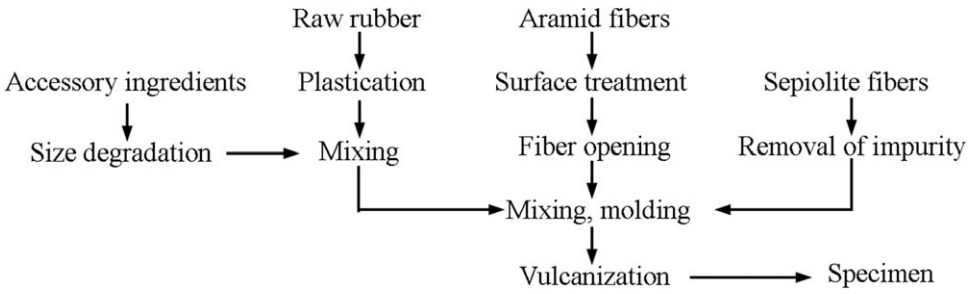

Figure 1. Molding process of SFRC.

Fiber Surface Treatments

The aramid fibers used in this study were subjected to two-step dip systems to improve the interfacial stress transfer between the fiber and the matrix. First, the aramid fibers were predipped in an epoxy compound with 5 wt % epoxy and dried at 200°C for 3 h. Then, the predipped aramid fibers were dipped in the RFL solution and dried at 200°C for 3 h.

A standard RFL solution was prepared in the following steps. First, the resorcinol solution was blended into the sodium hydroxide water solution. The solution was agitated for 5–10 min to dissolve the resorcinol. Then, the formaldehyde was added slowly to the resin solution. The RF solution was aged for 6 h at 25°C. Finally, the RF solution was added to a latex compound composed of the butadiene–vinyl pyridine copolymer latex and SB latex (L). The final RFL dip solution was aged for 20 h at 25°C. The components of the RFL latex system are given in Table III.

Processing

The sample were prepared through a molding process that was similar to that of traditional rubber-based composites,[28,29] as shown in Figure 1. The plastication was carried out with a mill mixer (XK160–320) to improve the plasticity of raw rubber. Before this step, raw rubber was roasted in a hot chamber within 333–343 K to decrease its hardness and improve manufacturability. The roll temperature of the mill mixer was controlled below 343 K, and the roller space was about 0.5–1 mm. The gross rubber was obtained in the mixing step, where all of the accessory ingredients and filling materials were dispersed evenly in the plasticity rubber by the repeated extrusion and shearing actions of the rollers.

The mixing step was also carried out in a mill mixer. During mixing, the reinforcing fiber was evenly dispersed in gross rubber, and the aspect ratio of the fiber was reduced to an appropriate value. The general orientation of the fibers was assumed to be in the milling direction, as reported by Senapati and coworkers.[8,30,31] The oriented samples were then piled into the compression mold by preservation of the fiber orientation and cured at 155°C for 20 min under pressure of 16 MPa on a heating press.

Testing

The dumbbell-shaped composite specimens in perpendicular directions with respect to the mill direction were die-cut from the compression-molded sheet, and the testing was done after 24 h of maturation at room temperature. The tensile properties were measured according to ASTM D 412-98A with a tensile testing machine (INSTRON 3367), and the average of three measurement results is reported. The fractured surfaces of the SFRC were analyzed with SEM (JSM-5900).

Testing Results

The transverse tensile strengths of the aramid fiber-reinforced rubber treated by the RFL latex and without surface treatment are shown in Table IV. After treatment by the RFL latex, the transverse tensile strength was improved by 84%.

The fractured surfaces of the developed SFRC of the SEM observation are shown in Figure 2. We observed that the surfaces of the aramid fibers without treatment were very smooth, and there were a few rubber particles adhering on the fiber surfaces. After the surface treatments of RFL, the adhesion effect between the fiber and rubber matrix was obviously improved.

ESTABLISHMENT OF A MICROMECHANICAL MODEL

Geometrical Model and Boundary Conditions

To predict the mechanical properties of the composites on the basis of the properties of the constituents, regular fiber packing is often assumed in computational simulations. Here, numerical homogenization was performed on a unit cell with hexagonal symmetry, on which the transversely isotropic behavior was simulated (Figure 3), where r denotes the radial component of the polar coordinate system. Using the package ABAQUS/Standard (2010), a two-dimensional finite element model made of isoparametric brick elements with four nodes was generated. Figure 3 shows a finite element mesh; this was strongly refined near the interfacial region. An element size of nearly $0.01r_f$, where r_f is the fiber radius, was used in the vicinity of the interface. Because of the symmetry of the unit cell and its constraints, only one-fourth of the unit cell needed to be modeled. The displacement boundary conditions, called *straight-line conditions*,[22] for transverse tension were expressed by eq. (1):

Table IV. Transverse Tensile Strength of the Aramid-Fiber-Reinforced Rubber

Type of fiber surface treatment	Without treatment	RFL
Transverse tensile strength (MPa)	5.90	10.62
	5.59	10.70
	5.93	10.77
Average value (MPa)	5.81	10.70

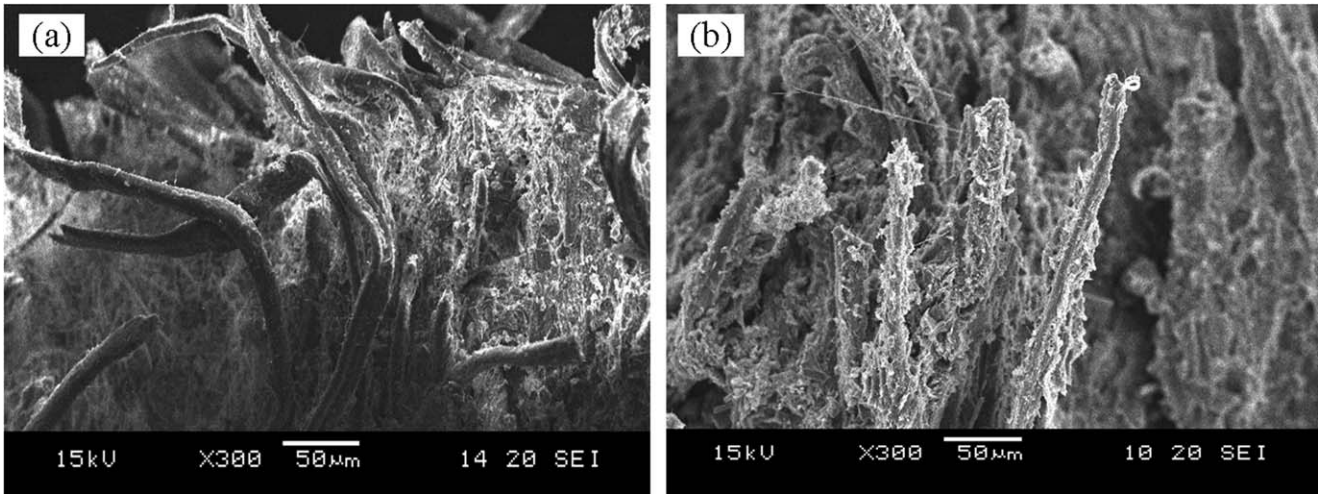

Figure 2. SEM photos of the transverse tensile fracture surfaces (a) without surface treatment and (b) after treatment by RFL latex.

$$\begin{aligned} u_x(0,y) &= 0 \\ u_x(a_1,y) &= -\delta_x \\ u_y(x,0) &= 0 \\ u_y(x,a_2) &= 0 = \delta_y \end{aligned} \tag{1}$$

where $a_1 = 10.4$ μm and $a_2 = 18$ μm, which are the geometric parameters shown in Figure 3. u_x and u_y are the displacements in the x and y direction, respectively. δ_y is a given displacement. δ_x is not known a priori and must be determined from the condition that the average normal forces acting on the planes $x = a_1$ is zero. It can be computed from eq. (2):

$$\int_0^{a_2} \sigma_x(a_1,y) = 0 \tag{2}$$

where σ_x is normal stress along x direction. The average transverse stress $\bar{\sigma}_y$ and strain $\bar{\varepsilon}_y$ over the RVE were computed by

$$\bar{\sigma}_y = \frac{1}{a_1}\int_0^{a_1} \sigma_y(x,a_2)dx, \quad \bar{\varepsilon}_y = \frac{\delta_y}{a_2} \tag{3}$$

Parameters of the Model

Dimensions of the three-phased unit cell with the hexagonal symmetry were chosen to respect values of $r_f = 6$ μm and fiber volume content = 30%. The elastic properties of the fiber, interphase, and matrix are given in Table V. The properties of the matrix were regard as a compound of those of sepiolite fibers and NBR because the size of the sepiolite fibers was much lower than that of aramid fiber and the major reinforcing phase in SFRC is the aramid fiber.

The mass ratio between aramid, sepiolite, and NBR in the composite was 28:49:21. Because the densities of aramid, sepiolite, and NBR were around 1.44, 2.10, and 1.00 g/cm^3, respectively. Their volume ratio was approximately 30:37:33. The tensile modulus of the matrix was 450 MPa; this value

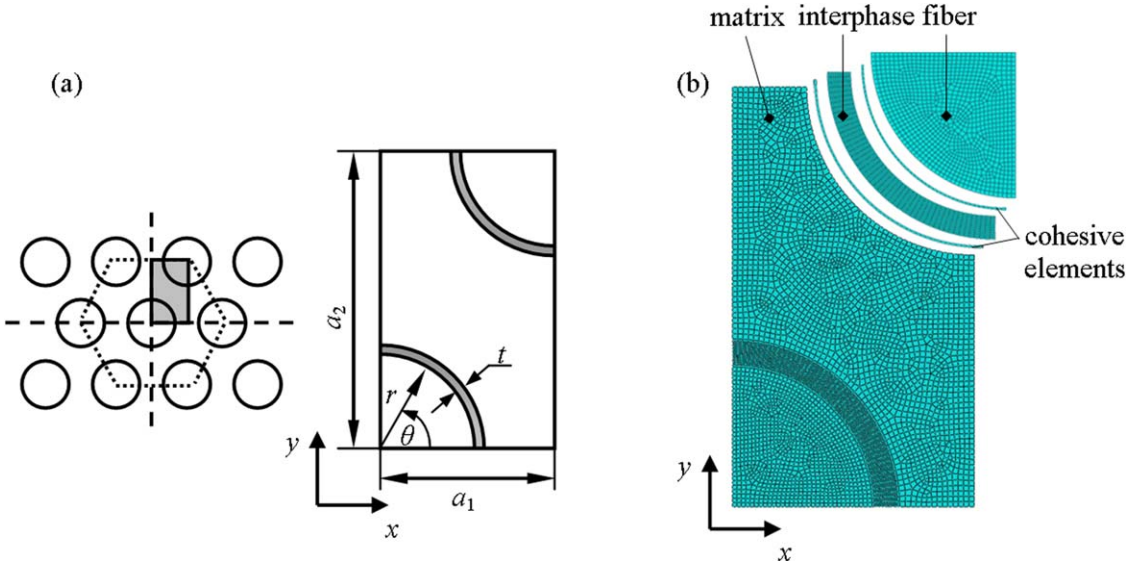

Figure 3. Micromechanics model: (a) one-fourth model of the RVE and (b) finite element discretization of the RVE. [Color figure can be viewed in the online issue, which is available at wileyonlinelibrary.com.]

Table V. Elastic Properties of the Constituents

Material parameter	Fiber	Matrix	Interphase
Young's modulus (MPa)	20000	450	50
Poisson's ratio	0.22	0.3	0.3

was obtained according to the stress–strain curves given by Takei *et al.*[32] If a sheet is subjected to a transverse tensile load, it is reasonable to assume that both the matrix and the interphase carry the load. The elastic properties of the interphase region differ from the respective one of the fiber and the matrix. The interphase thickness ($t = 1$ μm) was used in the numerical simulations presented in this article. The aforementioned value of t refers to the interphase thickness of the fiber-reinforced composites obtained from secondary ion mass spectroscopy[33] and atomic force microscopy.[34] The tensile modulus of the interphase was determined by the dry weight ratio of RF to L, as shown in Table VI.[35,36] The dry weight ratio of RF to L in this study was between 0.18 and 0.2; this corresponded to values of 41.52–62.76 MPa. So, an interphase modulus of 50 MPa was chosen for the following analysis.

Cohesive Zone Model

The micromechanical model includes two imperfect adhesions at the fiber/interphase (FI) interface and matrix/interphase (MI) interface. This formulation implies that debonding may occur at both interfaces. The cohesive zone model is used to describe the damage of the interface. The constitutive response of the cohesive element is defined in terms of a bilinear traction–separation law, which relates the separation displacement between the top and bottom faces of the element to the traction vector acting upon it. The initial response is linear in the absence of damage with an elastic stiffness of K. A value of $K = 10^5$ GPa/m was selected for the interface. The determination of its magnitude is primarily for numerical consideration; that is, it should be large enough to ensure the displacement continuity at the interface and to prevent any modification of the stress fields around the fibers in the absence of damage. Compared with a value of $K = 10^8$ GPa/m, we found that there was no obvious difference in the damage initiation and evolution processes.[24,25] The traction–separation law can be written as follows:

Table VI. Mechanical Properties of the RFL Films with Different Ratios of RF and L

RF/L	Tensile strength (MPa)	Elongation at break (%)	Tensile modulus (MPa)
8:100	2.69	52.86	5.09
10:100	3.58	47.86	7.48
12:100	4.56	41.53	10.98
14:100	6.06	37.59	16.12
18:100	8.47	20.37	41.52
20:100	11.88	20.93	62.76
25:100	14.84	15.93	93.16

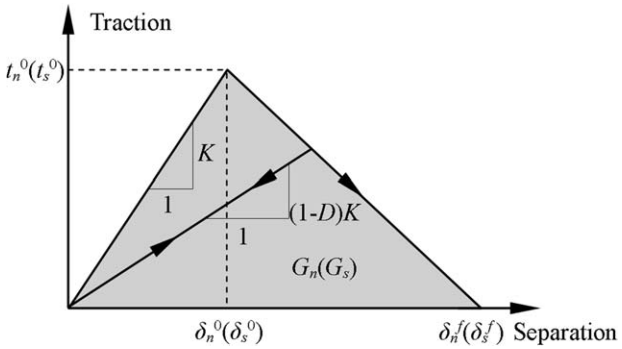

Figure 4. Traction–separation law of the cohesive element.

$$t_{n/s} = K\delta_{n/s} \tag{4}$$

Damage is assumed to be initiated when the maximum nominal stress ratio reaches one of the values given by following equation:

$$\max\left\{\frac{\langle t_n\rangle}{t_n^0}, \frac{t_s}{t_s^0}\right\} = 1 \tag{5}$$

where $\langle\ \rangle$ are the Macaulay brackets, which return the argument the value if positive and zero otherwise, to impede the development of damage when the interface is under compression. t_n^0 and t_s^0 are the interfacial normal and shear strengths. δ_n^0 and δ_s^0 are the interfacial normal and tangential displacement. G_n and G_s are the interfacial normal and tangential fracture energy. For simplicity, we assumed that t_n^0 is equal to t_s^0, that is, $t_n^0 = t_s^0$. Once the damage begins, the traction stress is reduced; this depends on the interfacial damage parameter (D), which evolves from 0 (in the absence of damage) to 1 (at ultimate failure), as shown in Figure 4. The displacement at failure (δ_n^f or δ_s^f) is determined by the interfacial fracture energy (G), which corresponds to the area under the traction–separation curve.

RESULTS AND DISCUSSION

Damage Initiation and Evolution

The previously proposed micromechanics model was used to simulate the softening behavior of the composite under transverse tension. The elastic properties of the constituents used in the analysis are summarized in Table V. The values of the interfacial strength and G were 10 MPa and 1 J/m^2, respectively. A comparison of the stress–strain curve between the simulation and experimental results is shown in Figure 5. The curve of the simulation results consisted of three portions, namely, the undamaged, transitional, and fully damaged portions; this represented the different responses of the material. The first and third portions had linear characteristics, whereas the second one showed nonlinear behavior. The sudden stress drop, known as the *snap-through instability,* was due to the stable debonding of the interface. During the snap-through process, the macro strain (ε) increased slightly with decreasing macro stress or maximum normal stress (σ_{22}) until the stiffness became positive again. The simulation result showed good agreement with the experimental results in the first and second portions. However, there was a difference in the third portion. The reason for this was that the damage of the matrix was not taken into consideration

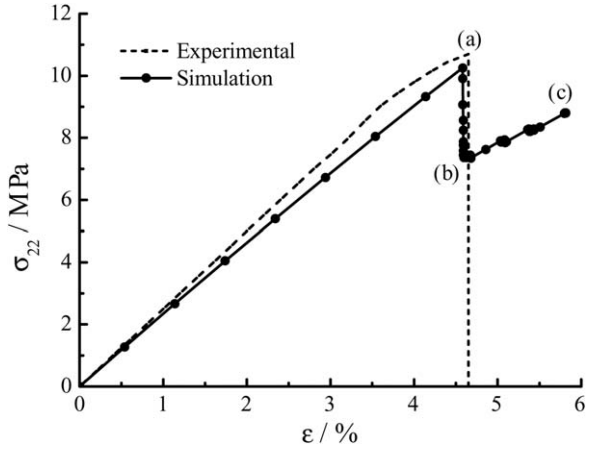

Figure 5. Comparison of the stress–strain curve between the simulation and experimental results.

in present model, and the matrix could carry the load after interfacial debonding.

Figure 6 shows the evolution of the cohesive tractions with increasing load as dependent on the polar angle (θ). It is interesting to note that the normal tensile cohesive traction (t_n) rose with increasing applied strain up to a level of 4.58%, as shown in Figure 6(a). The stress distributions at the FI and MI interfaces showed almost identical regularity, and the max stress was at the location $\theta = 90°$ at the interfaces. This means that for the two interfaces (FI and MI) with the aforementioned interfacial parameters, the debonding probability was the same. Figure 6(b) shows the stress distributions at the FI and MI interfaces after debonding. We found that debonding occurred at the MI interface. The interfacial debonding took place when ε was larger than 4.58%. The debonding length corresponded to the zone where t_n was equal to 0. The debonding length grew rapidly at a strain level from 4.58 to 4.60; this corresponded to the process from point a to b in Figure 5. Then, the debonding length increased slowly after the strain was larger than 4.60; this corresponded to the process from point b to c, as shown in Figure 5.

The stress field evolution and crack growth under transverse tension is shown clearly in Figure 7 at applied strain levels of 4.58, 4.60, and 5.81%, respectively. The first strain level (4.58%) corresponded to the debonding onset (point a, Figure 5). The second one corresponded to the end of the snap-through instability (point b, Figure 5), and in turn, the third one corresponded to point c in Figure 5. In fact, when $\varepsilon = 4.58\%$, because of stress concentration, t_n approached t_n^0, and the interfacial damage started to develop. A further load increase led to the steady growth of the crack, as shown in Figure 7(b). When the crack angle exceeded 60°, its propagation became stable, as shown in Figure 5 from point b to point c. σ_{22} occurred at the MI interface, as shown in Figure 7 (red circle), where the yield of the matrix most easily occurred. σ_{22} in the matrix was 24.27 MPa at $\theta = 0°$. With increasing macroscopic strain, σ_{22} decreased. However, when the debonding became stable, σ_{22} became large, and it occurred at the tip of the crack.

Parametrical Study of the Interface and Interphase

Influence of the Interfacial Strength. For the problem analyzed in this study, different t_n^0 values (8, 10, and 12 MPa) were considered to investigate the softening effect on the macroscopic material response. The value of G was 1 J/m^2. It is shown in Figure 8 that the value of t_n^0 had a strong influence on the softening behavior of the material. As shown by the increase in t_n^0 from 8 to 12 MPa for fixed values of other cohesive parameters, the peak values of the stress and strain in the stress–strain characteristics showed increases of about 57 and 61%, respectively. Therefore, we concluded that a higher interfacial strength enhanced the ductile behavior and strength of the material (Table IV).

Influence of *G*. The influence of G on the transverse deformation was also examined. Figure 9 illustrates the stress–strain response of the material when G increased form 1 to 4 J/m^2. The value of t_n^0 was 10 MPa. We observed that the peak stress rose slowly with increasing G. The stress–strain curves changed little when G varied from 1 to 2 J/m^2. When G reached 4 J/m^2, the failure strain rose markedly. So, the ductile properties of SFRC increased with increasing G.

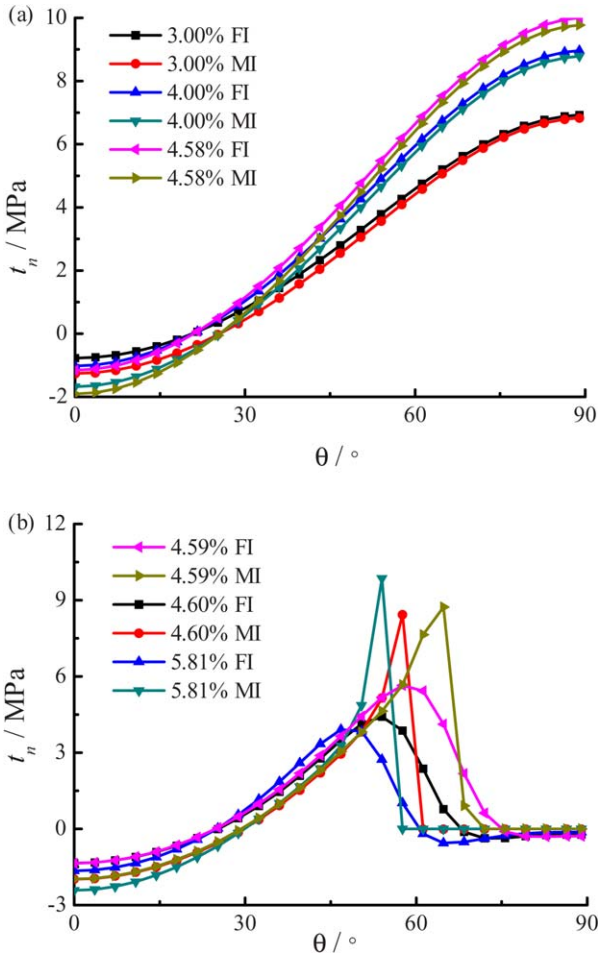

Figure 6. Angular distribution of t_n at the FI and MI interfaces: ε = (a) 3.00–4.58 and (b) 4.59–5.81%. [Color figure can be viewed in the online issue, which is available at wileyonlinelibrary.com.]

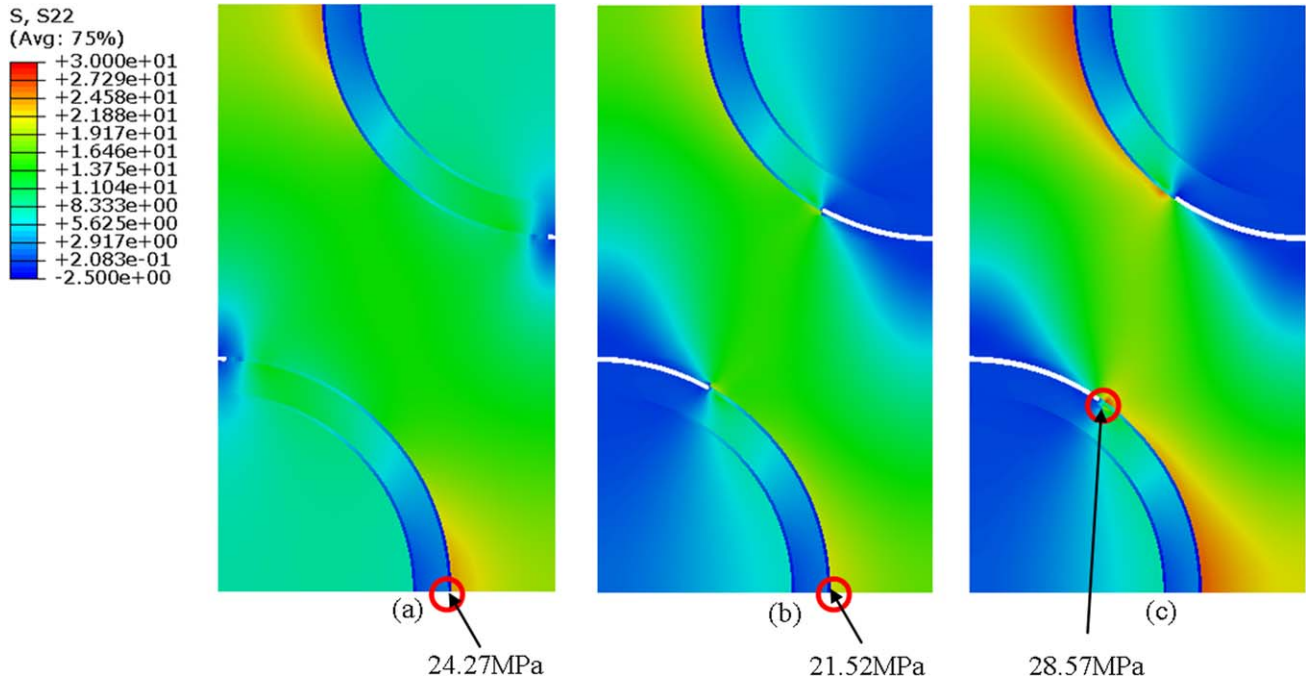

Figure 7. Damage initiation and evolution under transverse tension: $\varepsilon =$ (a) 4.58, (b) 4.60, and (c) 5.81%. [Color figure can be viewed in the online issue, which is available at wileyonlinelibrary.com.]

Effect of the Interphase Modulus. The effect of the interphase modulus on the properties of the material was investigated further for the selected values of t_n^0 and G, which were 10 MPa and 1 J/m^2, respectively. Figure 10 shows the macroscopic stress–strain curves for four different interphase moduli (40, 50, 60, and 80 MPa). A lower interphase modulus led to better ductile behavior and higher strength in the composite. However, a low interphase modulus corresponded to a low interphase tensile strength, as shown in Table VI; this caused interphase damage before interfacial debonding. The normal stress in the interphase is general greater than 8 MPa when interfacial debonding occurs. So, an interphase tensile strength larger than 8 MPa (corresponding to an interphase tensile modulus of ~40 MPa) was needed to ensure tensile strength of composite. Therefore, the choice of an interphase modulus between 40 and 50 MPa was optimal for the ductile behavior and strength of SFRC.

CONCLUSIONS

A composite material consisting of short aramid and sepiolite fibers in NBR was prepared and tested. The transverse tensile strengths of the SFRCs treated by RFL and without surface treatment were obtained. After treatment by the RFL latex, the transverse tensile strength was improved by 84%.

The micromechanical model developed here was used to simulate the evolution of damage of the SFRC and, furthermore, to predict the final failure of these materials. We found that the

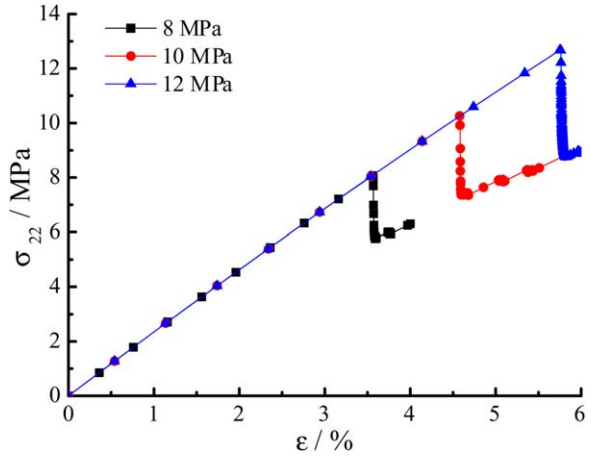

Figure 8. Macroscopic stress–strain curves for the SFRC under different interfacial strengths. [Color figure can be viewed in the online issue, which is available at wileyonlinelibrary.com.]

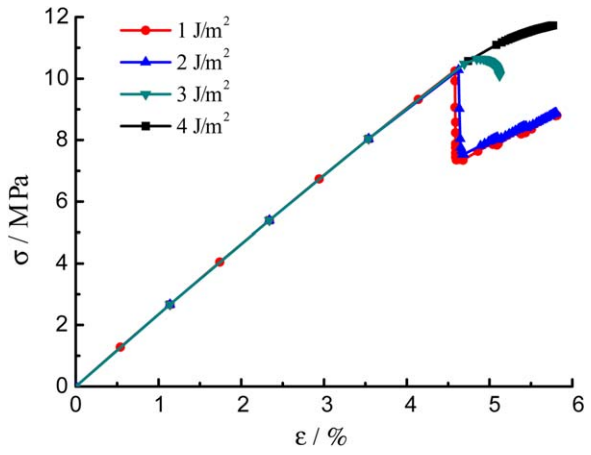

Figure 9. Macroscopic stress–strain curves for the SFRC for different G values. [Color figure can be viewed in the online issue, which is available at wileyonlinelibrary.com.]

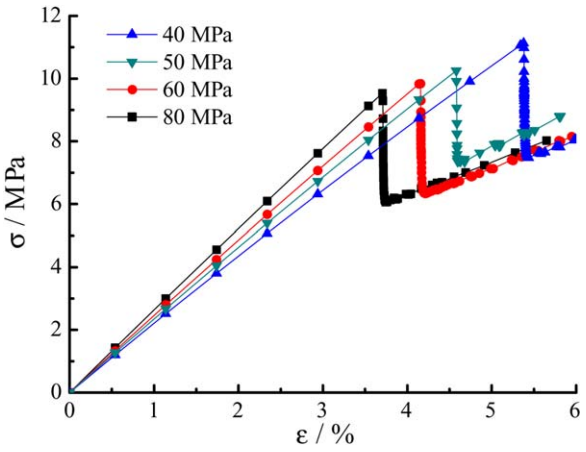

Figure 10. Macroscopic stress–strain curves for the SFRC for different interphase moduli. [Color figure can be viewed in the online issue, which is available at wileyonlinelibrary.com.]

predictions with the established model were in good agreement with experimental results when G was 1 J/m^2 and the interfacial strength was 10 MPa.

A parametrical study on the interface and interphase of the composite was conducted. When we increased t_n^0 from 8 to 12 MPa, the peak value of the stress and strain showed increases of about 57 and 61%, respectively. The ductile properties of SFRC also increased with increasing G. A choice of interphase modulus between 40 and 50 MPa was optimal for the ductile behavior and strength of SFRC.

ACKNOWLEDGMENTS

This project was supported by the National Natural Science Foundation of China (contract grant number 51375223) and Jiangsu Province Ordinary University Graduate Research and Innovation (contract grant number CXZZ11_0337).

REFERENCES

1. Vajrasthira, C.; Amornsakchai, T.; Bualek-Limcharoen, S. *J. Appl. Polym. Sci.* **2003**, *87*, 1059.
2. Kashani, M. R. *J. Appl. Polym. Sci.* **2009**, *113*, 1355.
3. Akbarian, M.; Hassanzadeh, S.; Moghri, M. *Polym. Adv. Technol.* **2008**, *19*, 1894.
4. Ahmad, I.; Wong, P. Y.; Abdullah, I. *Polym. Compos.* **2006**, *27*, 395.
5. Shibulal, G. S.; Naskar, K. *J. Appl. Polym. Sci.* **2013**, *128*, 4151.
6. Li, S.; Han, K.; Rong, H.; Li, X.; Yu, M. *J. Appl. Polym. Sci.* **2014**, 131, 40250.
7. Hintze, C.; Shirazi, M.; Wiessner, S.; Talma, A. G.; Heinrich, G.; Noordermeer, J. W. M. *Rubber Chem. Technol.* **2013**, *86*, 579.
8. Shirazi, M.; Talma, A. G.; Noordermeer, J. W. M. *J. Appl. Polym. Sci.* **2013**, *128*, 2255.
9. Coffey, A. B.; O'Bradaigh, C. M.; Young, R. J. *J. Mater. Sci.* **2007**, *42*, 8053.
10. Jamshidi, M.; Taromi, F. A. *J. Adhes. Sci. Technol.* **2007**, *21*, 169.
11. Yilmaz, B. *J. Adhes. Sci. Technol.* **2009**, *23*, 1893.
12. Wennekes, W. B. Ph.D. Thesis, University of Twente, **2008**.
13. de Lange, P. J.; Akker, P. G. *J. Adhes. Sci. Technol.* **2012**, *26*, 827.
14. Shibulal, G. S.; Naskar, K. *J. Polym. Res.* **2011**, *18*, 2295.
15. Shirazi, M.; Talma, A. G.; Noordermeer, J. W. M. *J. Adhes. Sci. Technol.* **2013**, *27*, 1048.
16. Shirazi, M.; de Rooij, M. B.; Talma, A. G.; Noordermeer, J. W. M. *J. Adhes. Sci. Technol.* **2013**, *27*, 1886.
17. Eichhorn, S. J.; Young, R. *J. Compos. Sci. Technol.* **2004**, *64*, 767.
18. Romanowicz, M. A. *Comp. Mater. Sci.* **2012**, *51*, 7.
19. López Jiménez, F.; Pellegrino, S. *Int. J. Solids Struct.* **2012**, *49*, 635.
20. Wu, L.; Tjahjanto, D.; Becker, G.; Makradi, A.; Jérusalem, A.; Noels, L. *Eng. Fract. Mech.* **2013**, *104*, 162.
21. Romanowicz, M. *Compos. A* **2010**, *41*, 1829.
22. Romanowicz, M. *Comp. Mater. Sci.* **2009**, *47*, 225.
23. Kushch, V. I.; Shmegera, S. V.; Brøndsted, P.; Mishnaevsky, L., Jr. *Int. J. Eng. Sci.* **2011**, *49*, 17.
24. Yang, L.; Yan, Y.; Liu, Y.; Ran, Z. *Compos. Sci. Technol.* **2012**, *72*, 1818.
25. Vaughan, T. J.; McCarthy, C. T. *Compos. Sci. Technol.* **2011**, *71*, 388.
26. Mishnaevsky, L., Jr.; Brøndsted, P. *Compos. Sci. Technol.* **2009**, *69*, 1036.
27. Koyanagi, J.; Sato, Y.; Sasayama, T.; Okabe, T.; Yoneyama, S. *Compos. A* **2014**, *56*, 136.
28. Tian, M.; Su, L.; Cai, W.; Yin, S.; Chen, Q.; Fong, H.; Zhang, L. *J. Appl. Polym. Sci.* **2011**, *120*, 1439.
29. Gu, B. Q.; Chen, Y.; Zhou, J. F. Advances in Composite Materials—Ecodesign and Analysis; Brahim, A., Ed.; InTech: Rijeka, Croatia, **2011**.
30. Senapaty, A. K.; Kutty, S. K. N.; Pradhan, B.; Nando, G. B. *Int. J. Polym. Mater.* **1989**, *12*, 203.
31. Hintze, C.; Boldt, R.; Wiessner, S.; Heinrich, G. *J. Appl. Polym. Sci.* **2013**, *130*, 1682.
32. Takei, T.; Oda, R.; Miura, A.; Kumada, N.; Kinomura, N.; Ohki, R.; Koshiyama, H. *Compos. B* **2013**, *44*, 260.
33. Thomason, J. L. *Composites* **1995**, *26*, 487.
34. Mai, K.; Mäder, E.; Mühle, M. *Compos. A* **1998**, *29*, 1111.
35. Shen, M. X.; Fei, C. J.; Xia, T. *Fiber Reinf. Plast. Compos.* **2006**, *4*, 20.
36. Shen, M. X.; Zhang, J. S.; Chen, Q. M. *J. Appl. Polym. Sci.* **2009**, *113*, 3550.